Absolute OH density measurements in a CO_2-H_2O glow discharge by laser-induced fluorescence spectroscopy

Absolute OH density measurements in a CO_2-H_2O glow discharge by laser-induced fluorescence spectroscopy

Maik Budde[1,2+], Luca Matteo Martini[1*], Matteo Ceppelli[3], Sara Quercetti[1*], and Richard Engeln[1]

[1]Department of Applied Physics, Eindhoven University of Technology, 5600 MB Eindhoven, The Netherlands

[2]Instituto de Plasmas e Fusão Nuclear, Instituto Superior Técnico, Universidade de Lisboa, Portugal

[3]Dipartimento di Fisica Università di Trento, Via Sommarive 14, 38123 Povo-Trento, Italy

[*]Present address: Dipartimento di Fisica Università di Trento, Via Sommarive 14, 38123 Povo-Trento, Italy

[+]Corresponding author

March 2022

Abstract

Time-resolved absolute OH density measurements in a millisecond-pulsed DC glow discharge from carbon dioxide with water admixture by laser-induced fluorescence (LIF) spectroscopy are presented. For that purpose, a novel technique is suggested to calibrate the OH LIF setup by means of two-photon absorption LIF spectroscopy measurements on a CO-filled gas cell. OH densities in the order of $1 \times 10^{18} \, \mathrm{m}^{-3}$ are reported at a pressure of $6.67 \, \mathrm{mbar}$ with a water admixture of 20% and a discharge current of $50 \, \mathrm{mA}$. Furthermore, the time evolution of the CO_2 conversion is determined from collision energy transfer LIF and validated against literature. The time-dependent rotational temperature of OH is obtained with LIF thermometry.

1   Introduction

With an increasing carbon dioxide concentration in the atmosphere and decreasing global resources of fossil fuels, the interest in the utilisation of CO_2 in the production of value-added chemicals is steadily growing. Low-temperature plasma appears to be a promising candidate for energy-efficient conversion of CO_2 in one of the production steps [1]. In addition to carbon monoxide the production of these value-added chemicals requires hydrogen as well. An abundant source of hydrogen is water. So-called *artificial photosynthesis* strives for the combined conversion of CO_2 and H_2O to syngas $(CO + H_2)$ or directly to compounds like ethanol [2]. Apart from exploiting the benefits of water addition its effect on carbon dioxide conversion must be considered anyway since water is an omnipresent impurity. For instance, the waste gas stream of a cement or power plant contains about 1% and 6% of water, respectively [3].

Regardless of the growing interest in artificial photosynthesis, the literature on combined plasmolysis of carbon dioxide and water is still scarce. The majority of studies suggests a negative effect, e.g. in the CO_2 laser community water is commonly added to the gas mixture to depopulate the lower laser level and to limit CO_2 decomposition [4–6]. On the contrary, also positive effects of water addition on CO_2 decomposition have been found. Chen et al. observed a decrease in gas temperature with water addition in a CO_2 microwave plasma which leads to higher conversion [7]. While most papers elaborate in great detail on the possibilities to optimise the processing with regard to distinct products, the direct influence of water on CO_2 splitting is rarely investigated. To further illuminate the processes in the CO_2-H_2O plasma, in situ investigations determining absolute number densities are required.

Two particularly important molecules are carbon monoxide and the hydroxyl radical. The former is the product of CO_2 decomposition while the latter is formed by water splitting. Both molecules can react according to

$$CO + OH \rightarrow \quad CO_2 + H \quad \text{and} \tag{1}$$

$$CO + OH \rightarrow \quad COOH. \tag{2}$$

The first reaction limits the effective conversion [8] while the latter appears to be an important step in the production of carboxylic acids [9].

Laser-induced fluorescence (LIF) spectroscopy has proven to be a powerful in situ diagnostic technique even in challenging environments [9–13]. With a proper calibration, absolute number densities can be determined with high temporal and spatial resolution [14]. The detection of CO with two-photon absorption laser-induced fluorescence (TALIF) spectroscopy is common practice in combustion research [15, 16] but has also been shown to be applicable in CO_2 plasma conversion studies [17].

In this study, TALIF spectroscopy on CO serves as an auxiliary diagnostic as will be detailed later. Martini et al. used OH as probe molecule to evaluate conversion in a carbon dioxide nanosecond repetitively pulsed plasma with a trace amount of water addition [10]. The applicability of OH LIF in a CO_2-H_2O plasma, shown by Martini et al., motivates the present study to focus on the OH radical itself with the goal of determining absolute number densities. Absolute numbers are crucial to assess the importance of reactions like eqs. (1) and (2) and to deepen the understanding of CO_2 conversion under realistic conditions. Additionally, absolute densities are expedient to benchmark plasma simulations [18].
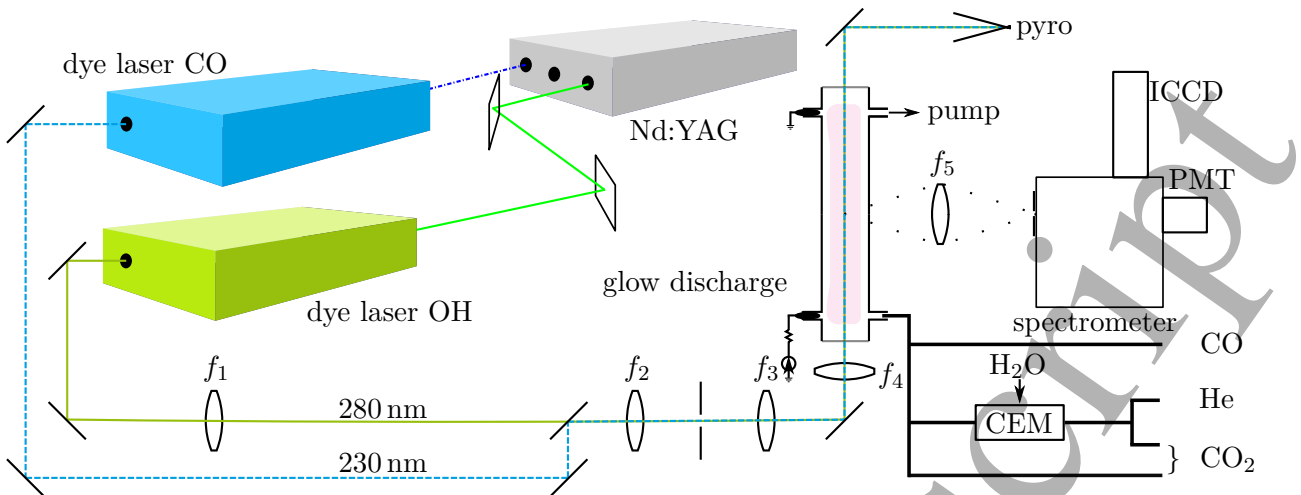
Figure 1: Schematic LIF setup where a Nd:YAG laser pumps two dye lasers to excite CO and OH molecules in a pulsed DC glow discharge. Emitted fluorescence light is collected at a 90° angle, spectrally dispersed in a spectrometer and detected by a PMT hooked to an oscilloscope or an ICCD camera. The f_i indicate the focal lengths of the used lenses that can be found in the text. The controlled evaporator mixer (CEM) is used to enrich either the He or the CO_2 gas flow with H_2O.

2 Setup

2.1 Excitation and detection system

The setup is schematically shown in fig. 1. The second and third harmonic of a Nd:YAG laser (Spectra Physics Quanta Ray PRO 290-30), externally triggered by a delay generator (Stanford Research Systems DG535) at 30 Hz, are used to pump two dye lasers (Sirah Precision Scan with Coumarin 460 dye in ethanol for CO, Sirah Cobra Stretch with Rhodamine 590 dye in ethanol for OH) to generate tunable laser radiation around 460 nm and 560 nm, accordingly. The laser light is frequency-doubled by a BBO or KDP crystal to obtain tunable laser radiation around 230 nm and 280 nm, respectively. The laser pulses show a nearly Gaussian profile in the time domain and have a duration (FWHM) of 5.9 ± 0.2 ns and 8.4 ± 0.2 ns as measured with the same fast photomultiplier tube used for the TALIF and LIF measurements, respectively. The spatial profiles of the laser beams are improved by a spatial filter consisting of a pinhole (diameter 50 μm) interposed between two positive lenses (focal length $f_{2,3} = 150$ mm). Another positive lens ($f_4 = 250$ mm) focuses the beams into the centre of the plasma reactor. The $1/e$-waist radius of the beams is determined to 100 μm by Gaussian beam propagation calculations starting from the pinhole of the spatial filter [19].

Fluorescence from the laser focus is collected at a 90° angle with a lens ($f_5 = 250$ mm) and imaged on the entrance slit of a spectrometer (Andor Shamrock SR-303i). A 2400 lines/mm grating (Jobin Yvon 53011) is used for wavelength selection. A motorised flipping mirror selects either a gated photomultiplier tube (PMT) (Hamamatsu H11526-20-NF) or a gated intensified charge-coupled device (ICCD) camera (Andor iStar) in full vertical binning to detect fluorescence light. The former is used to measure the time-resolved spectrally integrated fluorescence pulse, while the latter is used to measure the spectrally resolved fluorescence spectrum. The PMT signal is detected as a voltage drop over the 50 Ω resistor of a four-channel oscilloscope (Keysight DSOX3034T). The energy per laser pulse is measured simultaneously with the LIF signal with a pyroelectric detector (Gentec EO QS9-H), hence

fully accounting for pulse-to-pulse variations as the largest source of stochastic uncertainty, and can be adjusted for the CO laser with a Rochon prism and for the OH laser with a custom-made attenuator constructed from four wedges [20]. Stability of the lasers is ensured by a proper warm-up time and routinely monitoring the pulse energy with the pyroelectric detector, the temporal laser profile with a fast photodiode and the spectral profile by injecting part of the dye fundamental in a 10 GHz etalon (the latter two are not shown in fig. 1).

For calibration purposes the beams of the two dye lasers must be identical in path and spatial profile. By using a beamsplitter closely before the spatial filter an overlap between the two beams is realised and multiple irises along the way to the reactor allow to narrow them down to one path. The mentioned spatial filter is then not only used to improve the beam profile significantly but also to match the profiles of the two beams. The slightly stronger divergence of the beam of the OH dye laser compared to the CO dye laser is compensated with a lens with long focal length ($f_1 = 5000$ mm) as shown in fig. 1.

2.2 Plasma setup

The reactor is a 23 cm long Pyrex cylinder with an inner diameter of about 2 cm, presented in fig. 1. The inter-electrode distance is 17 cm. Gas inlet and outlet are equally spaced and form a 90° angle with high-voltage and grounded electrode, respectively. The high-voltage electrode is connected to a high-power voltage amplifier (Trek 10/40A-HS), driven in voltage-controlled mode, in series with a 50 kΩ resistor to prevent arcing. The amplifier is controlled by a waveform generator (HP 33120A) that is triggered to match the laser cycle at 30 Hz with the 60 Hz plasma cycle consisting of 5 ms on - 11.67 ms off time. This specific duty cycle was, just like the operating pressure of 6.67 mbar, chosen according to earlier measurements [17, 21]. In this configuration the cylinder is filled only with the positive column of the glow discharge.

The gas-feed system delivers CO (Linde 4.5 Instrument, 99.995 % purity), CO_2 (Linde 4.5 Instrument, 99.995 % purity) or He (Linde 5.0 Detector, 99.999 % purity) to the reactor. The flows are supplied by mass flow controllers (Bronkhorst F-201CV). Water is added to the He or CO_2 line by guiding the gas streams through a controlled evaporator mixer (Bronkhorst W-101A) that is connected to a deionized water reservoir. The water is evaporated in the heat exchanger of the device heated to 120 °C thereby humidifying the gas stream. The gas lines are not further heated. Water condensation is prevented by keeping the water partial pressure in the lines below the equilibrium vapour pressure. The pressure in the reactor is kept constant by automatically adjusting the effective pumping speed of a dry roots pump (Pfeiffer ACP 15) through control of an automatic valve (Pfeiffer EVR 116), a feedback controller (Pfeiffer RVC 300), and a pressure gauge (Pfeiffer CMR 263).

3 Spectroscopic background

To get quantitative results from LIF spectroscopy, the selection of a proper excitation-relaxation or LIF scheme that includes all levels that are involved in the LIF process is essential. The time-dependent population densities $n_i(t)$ of these states i need to be calculated. They are determined by setting up and solving a system of rate equations that describes the radiative and non-radiative processes. For this purpose, in fig. 2 the potential energy curves for CO and OH are shown [22, 23] together with the used LIF schemes described below.

3.1 CO TALIF Modelling

The CO molecules in the ground state $CO(X^1\Sigma^+, v'' = 0)$ get excited by two-photon absorption around 230 nm to the $CO(B^1\Sigma^+, v' = 0)$ state. From there molecules can relax radiatively to lower energetic states. The spontaneous emission to the $CO(A^1\Pi, v = 2)$ state around 520 nm is selected as observable of the TALIF experiment [17]. The excitation-relaxation scheme is therefore

$$CO(X^1\Sigma^+, v'' = 0) + 2h\nu_L \rightarrow CO(B^1\Sigma^+, v' = 0) \rightarrow CO(A^1\Pi, v = 2) + h\nu_{BA}, \qquad (3)$$
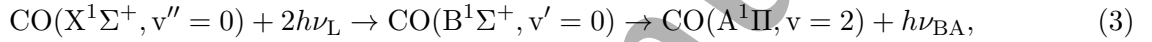
with v being the vibrational quantum number, h the Planck constant, ν_L the laser frequency and ν_{BA} the frequency of the emitted fluorescence photon. As experimentally confirmed, the fluorescence signal scales linearly with the square of the energy per pulse ε_p. Photoionization and depletion of the ground state can for that reason be neglected. The LIF process is satisfactorily described by a three-level model leading to [24]

$$n_B(t) = n_X e^{-\frac{t}{\tau}} \int_0^t R_{XB}(t') e^{\frac{t'}{\tau}} dt', \qquad (4)$$

where n_X and n_B are the population densities of the ground and the excited state, respectively, τ is the effective lifetime of the excited state and

$$R_{XB}(t) = \sigma^{(2)} \Psi G^{(2)} \left(\frac{\varepsilon_p F(t)}{h\nu_L \tilde{A}} \right)^2 \qquad (5)$$

the two-photon excitation rate. Here $\sigma^{(2)} = 1.5 \pm 0.5 \times 10^{-43}\,\mathrm{m}^4$ is the spectrally integrated two-photon excitation cross section with symmetrized error margin taken from literature [25]. Ψ is the spectral overlap integral defined as convolution $\Psi = a(2\nu - \nu_{XB}) * l(\nu - \nu_L) * l(\nu - \nu_L)$ with a being the normalised absorbing line profile around transition frequency ν_{XB} and l the normalised laser line shape [24]. The overlap integral is calculated according to McKenzie and Gross [26] using calculated values for Doppler and pressure broadening [27] and extracting the instrumental broadening from a fitting script for the CO TALIF excitation spectrum developed by Damen et al. [17]. Furthermore, $G^{(2)} = 2$ is the second order correlation factor for a multi-mode laser like the used dye laser, $F(t)$ the measured normalised laser time profile and $\tilde{A}$ the calculated laser beam area [24]. It should be noted that the energy per laser pulse in eq. (5), ε_p, is calculated from the average over multiple laser shots to improve the signal-to-noise ratio. This approach is not rigorous since the average of the squared laser energy per pulse, $\langle \varepsilon_p^2 \rangle$, should be considered instead of $\langle \varepsilon_p \rangle^2$ in eq. (5). Since the pulse-to-pulse energy is a quasi-stochastic variable, $\langle \varepsilon_p^2 \rangle$ can be derived from $\langle \varepsilon_p \rangle^2$ and the variance of ε_p $(\mathrm{Var}(\varepsilon_p) = \langle \varepsilon_p^2 \rangle - \langle \varepsilon_p \rangle^2)$. In

3 SPECTROSCOPIC BACKGROUND   6
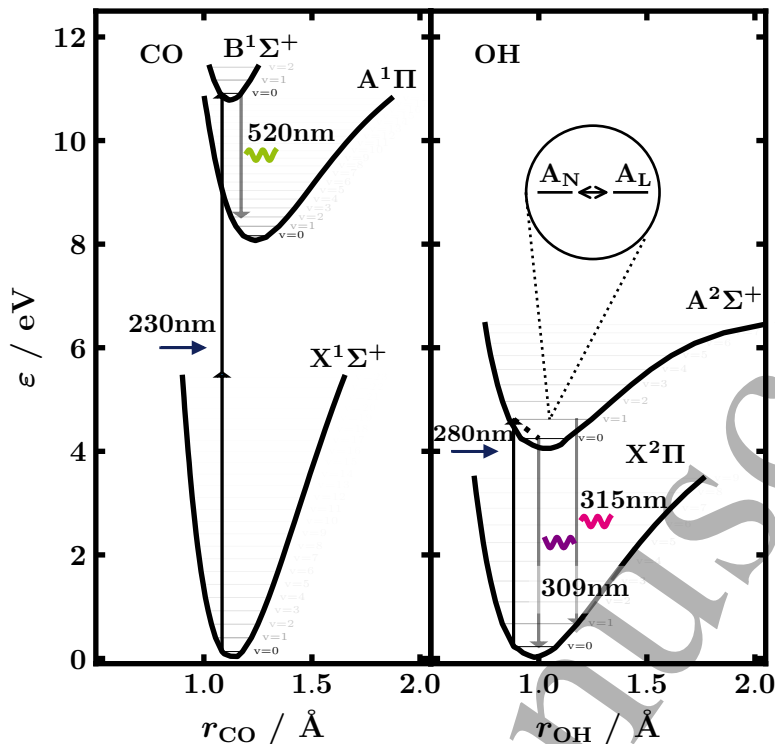

Figure 2: Potential energy curves of CO [22] and OH [23] that also include the (TA)LIF scheme for each molecule. CO excitation takes place in the Hopfield-Birge system while fluorescence in the Ångstrom system is the selected observable [17]. For OH the 3064 Å system is chosen [28]. Vibrational energy levels are sketched within the energy curves. Horizontal arrows represent the exciting laser photons and their wavelengths. Vertical arrows indicate transitions between energy levels. The emitted fluorescence photons are indicated by a wavelength and a wavy line. For OH also transitions between rotational levels A_N and A_L are shown.

our experimental conditions, $\mathrm{Var}(\varepsilon_p)$ accounts for $21\,\%$ of $\langle\varepsilon_p\rangle^2$. To be consistent with the derivation of $\sigma^{(2)}$ by Di Rosa and Farrow, this correction is not implemented in eq. (5). Indeed, in [25], $\sigma^{(2)}$ is determined by computing the irradiance starting from the square of the average of the energy per pulse (with a $\mathrm{Var}(\varepsilon_p) = 22\,\%$ of $\langle\varepsilon_p\rangle^2$). Continuously monitoring the beam, especially the energy per laser pulse, simultaneously with the fluorescence allows us to properly estimate the contributions of Ψ, F, ν_L, $\tilde{A}$ and ε_p to the final uncertainty of the resulting calibration constant, see section 4.1 for the discussion on the most relevant error sources. Used rates/rate coefficients are summarised in table 1.

3.2 OH LIF Modelling

For LIF on OH we adopt the five-level model described by Dilecce et al. [28] which is briefly explained in the following. In contrast to CO, the rotational lines of OH are spectrally spaced so far apart with respect to the narrow laser linewidth that excitation of a single rovibronic transition is possible. The $\mathrm{OH}(\Sigma)$ states are described by Hund's case (b). The same nomenclature is used for the other states with a finite orbital angular momentum along the internuclear axis that lay between case (a) and (b)

3   SPECTROSCOPIC BACKGROUND   7

[29]. According to this notation and fig. 2 the used LIF scheme is

$$OH(X^2\Pi, v'' = 0, N'') + h\nu_L \rightarrow OH(A^2\Sigma^+, v' = 1, N') \rightarrow OH(X^2\Pi, v = 1) + h\nu_{(1,1)}. \quad (6)$$
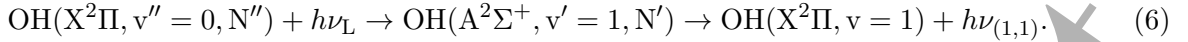
v is the vibrational quantum state and N the angular momentum apart from electron spin [29]. Again h is the Planck constant and ν_L the tunable frequency of the exciting laser with a wavelength around $\lambda = 280$ nm. $\nu_{(1,1)}$ is the frequency of the fluorescence light emitted by the laser-excited state and other rotational levels populated by rotational energy transfer (RET), corresponding to a wavelength around 315 nm. Due to vibrational energy transfer (VET) from $OH(A^2\Sigma^+, v' = 1)$ to the $OH(A^2\Sigma^+, \tilde{v}' = 0)$ manifold

$$OH(A^2\Sigma^+, \tilde{v}' = 0) \rightarrow OH(X^2\Pi, \tilde{v} = 0) + h\nu_{(0,0)} \quad (7)$$

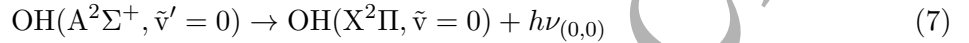is observed simultaneously, around 309 nm [10]. The five-level model simulates the time evolution of the population of the levels relevant for the LIF process. Specifically, the rotational levels $OH(X^2\Pi, v'' = 0, N'')$ and $OH(A^2\Sigma^+, v' = 1, N')$ interacting with the laser radiation and the vibrational level populated by VET $OH(A^2\Sigma^+, \tilde{v}' = 0)$ are included. In addition, the other rotational levels of the $OH(X^2\Pi, v'' = 0)$ and $OH(A^2\Sigma^+, v' = 1)$ manifold are considered, since they exchange population through RET with the $OH(X^2\Pi, v'' = 0, N'')$ and $OH(A^2\Sigma^+, v' = 1, N')$ levels, respectively. These other rotational levels are included in the model as two effective states, i.e. the *lumped* states, that reproduce the behaviour of the whole manifold, excluding $OH(X, v'' = 0, N'')$ and $OH(A^2\Sigma^+, v' = 1, N')$ [28]. For the upper state this is represented in fig. 2 by A_N, corresponding to the laser-populated level $OH(A^2\Sigma^+, v' = 1, N')$, and A_L, representing the lumped state. Verreycken et al. compared a four- and a six-level model, finding only minor differences between the two [30], making the five-level model a reasonable choice.

For each experimental condition the model is solved numerically by a custom Python script which takes as input (i) the time-resolved spectrally integrated fluorescence pulse (collected with the PMT) of OH, S, i.e. the quantity to be fitted, and (ii) the ratio, r_B, of the spectral integrals of the time-integrated fluorescence spectrum (collected with the ICCD camera) of the (1,1) and (0,0) band, i.e. $I_{(1,1)}$ and $I_{(0,0)}$, respectively. While S gives information about the total OH density, r_B depends on the gas composition [31]. This band ratio can be calculated as

$$r_B = \frac{I_{(0,0)}}{I_{(1,1)}} = \frac{A_{(0,0)}}{A_{(1,1)}} \frac{\sum_{i=1}^m \chi_i K_{VET}^i}{\sum_{i=1}^m \chi_i K_{Q0}^i + A_0}. \quad (8)$$

Here $A_{(v',v)}$ are the effective Einstein emission coefficients for transitions between $OH(A^2\Sigma^+, v')$ and $OH(X^2\Pi, v)$ with v' and v being 0 or 1. χ_i is the molar fraction of the i-th gas in a mixture of m gases, K_{VET}^i the rate for vibrational energy transfer by gas i, K_{Q0}^i the non-radiative quenching rate of level $OH(A^2\Sigma^+, \tilde{v}' = 0)$ by gas i and A_0 the total radiative depopulation rate for the $OH(A^2\Sigma^+, \tilde{v}' = 0)$ state, defined as $A_0 = \sum_{j\neq 0} A_{0j}$, where the A_{0j} are the Einstein coefficients for individual radiative transitions from that state [31].

The methodology of deducing information about the gas composition from its influence on the shape of the OH fluorescence spectrum, introduced as collision energy transfer (CET) LIF by Martini et al. [9], is not entirely impartial in the sense that assumptions regarding the formed products are required which are presented and justified in the following.

3 SPECTROSCOPIC BACKGROUND

In the present work a CO_2-H_2O gas mixture is treated in the plasma. The splitting of water is considered negligible for two reasons. Firstly, earlier studies found a conservation of the carbon balance meaning that no hydrocarbons are deposited [32]. Consequently, no water is decomposed for their formation [33]. Secondly, the measured OH density supports the assumption retrospectively as it corresponds to a low average hydroxyl-to-water ratio in the order of 0.01%.

For CO_2 this is different. The initial carbon dioxide is partly converted to CO and O_2, according to the reaction $CO_2 \rightarrow CO + O$ followed by the recombination of the oxygen atoms or the reaction with excited carbon dioxide $O + CO_2^* \rightarrow CO + O_2$ [34], i.e. in total $2CO_2 \rightarrow 2CO + O_2$. The conversion α is defined as

$$\alpha = \frac{\rho_{CO}}{\rho_{CO} + \rho_{CO_2}}, \tag{9}$$

where ρ_{CO} and ρ_{CO_2} are the number densities of CO and CO_2, respectively. The gas fractions of the involved species after conversion are then

$$\chi_{H_2O}^{final} = \frac{\chi_{H_2O}}{\chi_{H_2O} + (1 + \frac{\alpha}{2})\chi_{CO_2}}, \qquad \chi_{CO_2}^{final} = \frac{(1-\alpha)\chi_{CO_2}}{\chi_{H_2O} + (1 + \frac{\alpha}{2})\chi_{CO_2}},$$

$$\chi_{CO}^{final} = \frac{\alpha\chi_{CO_2}}{\chi_{H_2O} + (1 + \frac{\alpha}{2})\chi_{CO_2}} \qquad \text{and} \qquad \chi_{O_2}^{final} = \frac{\frac{\alpha}{2}\chi_{CO_2}}{\chi_{H_2O} + (1 + \frac{\alpha}{2})\chi_{CO_2}}. \tag{10}$$

χ_{H_2O} and χ_{CO_2} are the initially set molar fractions of water and carbon dioxide, respectively. In conclusion, by taking the band ratio as an input parameter, the conversion can be calculated from eq. (8). The ratio is determined from fits of the two bands of the background-corrected fluorescence spectrum measured with the ICCD camera with another custom Python code, see fig. 5c). The spectrum is fitted by adjusting the populations of the different rotational levels, hence fully accounting for a non-thermal rotational population distribution.

The quantification of LIF is substantially affected by the rotational population distribution, since the rates for quenching and VET are state-to-state dependent, which demands a few more elaborations regarding the used rate coefficients. We emphasise that in the case of OH due to the narrow laser linewidth only one single rotational level in $OH(A^2\Sigma^+, v' = 1)$ is populated leading to a nascent rotational population distribution far from thermal equilibrium. As indicated in fig. 2 the population can be redistributed among all rotational levels by RET. If a sufficient number of collisions is experienced by the excited OH molecules, thermal equilibrium can be achieved and the rotational population distribution of $OH(A^2\Sigma^+, v' = 1)$ is given by a Boltzmann distribution. A prerequisite for thermal equilibrium is that the vibronic parent level experiences enough collisions before it gets depopulated by (non-)radiative decay [35]. This means, quantitatively that the RET rate must be bigger than the rate of de-excitation of the excited state. However, in a molecular gas this is often not the case. Due to the aforementioned state-to-state dependence, the rates for a nascent distribution are quite different from those for a broader thermal distribution after a sufficient number of collisions. Therefore, depending on the situation, either thermal [36] or non-thermal rate coefficients [35] are used in the calculation of the fluorescence pulse and the conversion. The temperature required for the calculation of the non-thermal rate coefficients is obtained from the simulation of the excitation spectrum of OH with the LIFBASE tool [27]. Analogously to eq. (5), the spectral overlap integral is required for the calculations. It is determined from the excitation spectrum of the isolated $P_1(3)$ line [28]. Used rates/rate coefficients are summarised in table 1.

3 SPECTROSCOPIC BACKGROUND

Table 1: Overview of used rates (A for Einstein emission coefficients and K for collisional rates) in s^{-1}, rate coefficients k in $\mathrm{cm}^3\,\mathrm{s}^{-1}$ and stimulated emission/absorption coefficient B in $\mathrm{m}^2\,\mathrm{J}^{-1}\,\mathrm{s}^{-1}$ for the excited species CO and OH. OH rate coefficients are non-thermal if not indicated otherwise by a superscript th. The calculation of rate coefficients according to the given formulas can require the reduced mass of the collision process μ in kg and the temperature T in K. * Only valid in thermal situation. In the non-thermal case Einstein emission coefficients for individual transitions should be weighted by the corresponding rotational level populations.

Species	Collider	Symbol	Value					Ref.
CO		A_{BX}	31×10^6					[37]
		A_{BA}	13×10^6					[37]
			$\sigma_0 (T/293)^n \sqrt{8/(\pi \mu k_{\mathrm{B}} T)}$					
			σ_0				n	
	CO	k_{CO}	36.69×10^{-20}				0.02	[38]
	He	k_{He}	0.25×10^{-20}				1	[38]
OH		$A_{(0,0)}$	$1.451 \times 10^6 *$					[27]
		$A_{(1,1)}$	$8.678 \times 10^5 *$					[27]
		$K_{\mathrm{RET,X}}$	4.0×10^9					[28]
		$K_{\mathrm{RET,A}}$	3.3×10^9					[28]
		B	5.351×10^8					[27]
	He	$k_{\mathrm{Q0}}^{\mathrm{He,th}}$	4.0×10^{-14}					[36]
	He	$k_{\mathrm{Q1}}^{\mathrm{He,th}}$	4.0×10^{-14}					[36]
	H_2O	$k_{\mathrm{Q0}}^{\mathrm{H_2O,th}}$	65.6×10^{-11}					[36]
	H_2O	$k_{\mathrm{Q1}}^{\mathrm{H_2O,th}}$	60.6×10^{-11}					[36]
	He	$k_{\mathrm{VET}}^{\mathrm{He,th}}$	2.0×10^{-14}					[36]
	H_2O	$k_{\mathrm{VET}}^{\mathrm{H_2O,th}}$	7.3×10^{-11}					[39]
			$d\sqrt{T}(a\exp(-\epsilon_1 T) + b\exp(-\epsilon_2 T))$					
			a	b	ϵ_1	ϵ_2	d	
	CO_2	$k_{\mathrm{Q0}}^{\mathrm{CO_2}}$	29.73	16.87	3.10×10^{-3}	3.05×10^{-4}	4.15×10^{-13}	[35]
	CO_2	$k_{\mathrm{Q1}}^{\mathrm{CO_2}}$	95.80	64.24	3.30×10^{-3}	1.83×10^{-4}	4.15×10^{-13}	[35]
	O_2	$k_{\mathrm{Q0}}^{\mathrm{O_2}}$	14.59	6.11	4.87×10^{-3}	4.80×10^{-4}	4.37×10^{-13}	[35]
	O_2	$k_{\mathrm{Q1}}^{\mathrm{O_2}}$	27.59	18.16	3.04×10^{-3}	1.88×10^{-4}	4.37×10^{-13}	[35]
	CO	$k_{\mathrm{Q0}}^{\mathrm{CO}}$	26.42	16.44	2.72×10^{-3}	2.66×10^{-4}	4.47×10^{-13}	[35]
	CO	$k_{\mathrm{Q1}}^{\mathrm{CO}}$	60.24	22.78	2.34×10^{-3}	0.30×10^{-4}	4.47×10^{-13}	[35]
	H_2O	$k_{\mathrm{Q0}}^{\mathrm{H_2O}}$	43.56	21.64	2.35×10^{-3}	1.14×10^{-4}	4.92×10^{-13}	[35]
	H_2O	$k_{\mathrm{Q1}}^{\mathrm{H_2O}}$	60.61	34.61	1.96×10^{-3}	0.84×10^{-4}	4.92×10^{-13}	[35]
	CO_2	$k_{\mathrm{VET}}^{\mathrm{CO_2}}$	33.67	20.47	3.14×10^{-3}	1.72×10^{-4}	4.15×10^{-13}	[35]
	O_2	$k_{\mathrm{VET}}^{\mathrm{O_2}}$	2.50	1.44	2.75×10^{-3}	2.10×10^{-4}	4.37×10^{-13}	[35]
	CO	$k_{\mathrm{VET}}^{\mathrm{CO}}$	10.21	3.31	2.17×10^{-3}	0.41×10^{-4}	4.47×10^{-13}	[35]
	H_2O	$k_{\mathrm{VET}}^{\mathrm{H_2O}}$	5.47	2.92	2.12×10^{-3}	0.15×10^{-4}	4.92×10^{-13}	[35]

3.3 Calibration

To get absolute number densities, time-dependent LIF fluorescence pulses $S(t)$ are measured with the oscilloscope and calculated as

$$S_{\text{CO}}(t) = C_{\text{CO}} A_{(0,2)} n_{\text{B}}(t) \quad \text{and} \quad S_{\text{OH}}(t) = C_{\text{OH}}(A_{(0,0)} n_{\text{A0}}(t) + A_{(1,1)} n_{\text{A1}}(t)) \tag{11}$$

for CO TALIF and OH LIF, respectively. Here $A_{(v',v)}$ is again the effective Einstein emission coefficient for the observed band from vibrational level v′ in the excited state to vibrational level v in the lower state. n_i is the time-dependent population density of the emitting state with n_{B} calculated from eq. (4), n_{A0} and n_{A1} determined from the five-level model (n_{A1} is the sum of the populations in the A_{N} and A_{L} states in fig. 2) and C_X with X=CO,OH is the calibration constant [40]. The latter (in $V\,m^3\,s$) incorporates the sampled volume, i.e. the intersection of the laser beam with the slit image of the spectrometer as projected by the collection optics. C_X is usually determined from a chemical model [11], another diagnostic that relies on the same calibration constant [24] or a calibration source [41]. Here the last two options are combined. Specifically, a combination of TALIF on CO and LIF on OH is used to build a calibration source according to the following method. In a first step the two dye laser beams are made as identical as possible by a thorough alignment, compare fig. 1 and the elaborations at the end of section 2.1. The calibration constant is hence assumed to be identical for TALIF and LIF experiments. A correction factor is applied to take into account differences in transmission/reflection efficiency of the collection optics, grating and PMT photocathode quantum efficiency at 310 nm with respect to 520 nm as taken from the manufacturers' specification sheets.

The reactor is filled with CO without igniting a plasma. From temperature and pressure, the absolute number density of carbon monoxide is calculated. The CO density is kept as low as possible ($1.3\pm0.3\times 10^{21}\,m^{-3}$ assuming dynamic dilution) by diluting with 50 mbar of helium which is needed to reduce the partial pressure of CO while simultaneously limiting the diffusion of CO(B), i.e. CO molecules should not escape the probed volume during the lifetime of the excited state. Helium is chemically inert, and its quenching rates are negligible [37]. C_{CO} is determined by modelling the fluorescence pulse with eq. (4) and using eq. (11).

As OH calibration source, the reactor is filled with a mixture of helium and water and the plasma is ignited. The OH that is formed is determined with LIF spectroscopy by modelling the measured fluorescence pulse with the five-level model. With the calibration constant from above, the absolute OH number density is calculated. For the given He and H_2O flow, discharge current and pressure, the OH production is found to be reproducible. This shows that the glow discharge apparatus can be used as a calibration source for OH LIF. To improve the signal-to-noise ratio, the time-resolved fluorescence pulse and the beam energy are measured by averaging successive laser pulses with the excitation laser set to the Hopfield-Birge system band head at 115.05 nm or to the $P_1(3)$ at 283.01 nm, for TALIF on CO or LIF on OH, respectively.
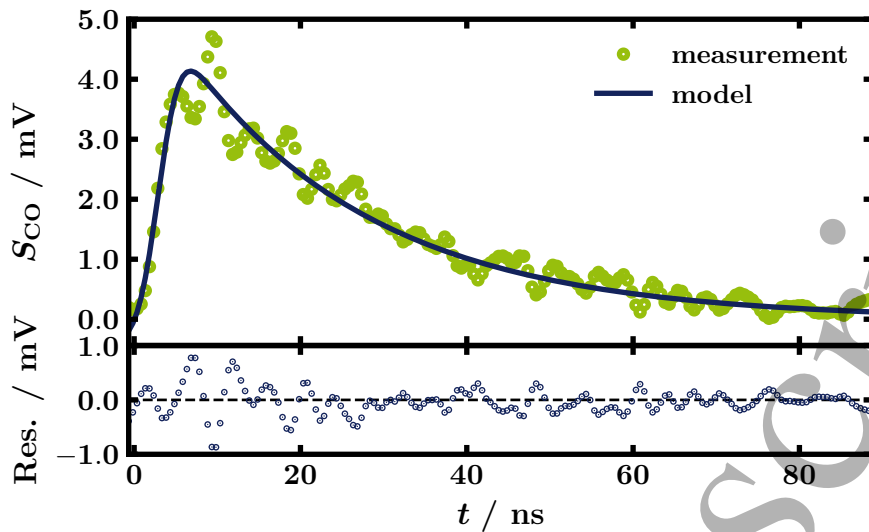
Figure 3: Fit of the measured fluorescence pulse of CO with the developed model from eqs. (4) and (11). The lower panel shows the residual.

4   Results

4.1   Determination of the calibration constant

The calibration constant is determined by measuring the PMT signal S_{CO} of about 1000 ppm CO in 50 mbar He at room temperature and fitting it with eq. (11) as shown in fig. 3. The pulse is satisfactorily fitted with the model as can be seen from the residual in the lower panel of fig. 3, thereby emphasising the validity of the three-level model.

From fitting the function in eq. (11) to the measured TALIF pulse, a calibration constant of

$$C_{CO} = 5 \pm 3 \times 10^{-26}\,\mathrm{V\,m^3\,s}$$

is obtained. The uncertainty is caused to a large extend by the two-photon excitation cross section of Di Rosa and Farrow [25] that is nowadays still the commonly used one [15]. Beside the uncertainty on $\sigma^{(2)}$, as anticipated in section 3.1, the two-photon nature of TALIF requires particular care in the estimation of ε_p, $F(t)$ and $\tilde{A}$, since differences with respect to the *real*, i.e. laser shot-dependent, quantities do not cancel as they would with a single-photon calibration method. Specifically:

- ε_p: The accuracy of the estimation of ε_p is 5 %, resulting in an uncertainty of 10 % on C_{CO}.

- $F(t)$: Variations of the temporal profile of the laser or the use of a laser pulse profile $F(t)$ that differs from the real one have an incidence in the estimation of R_{XB} and can translate in a statistic or systematic error, respectively. A deviation of 1 ns of the FWHM, for example, would change the estimation of C_{CO} by 7 %. The accuracy in measuring $F(t)$ is mainly due to the bandwidth of the oscilloscope (350 MHz) used to acquire the time profile of the signal through the PMT (rise time 0.57 ns). In the present case, it can be estimated as 0.2 ns, which results in a 1.4 % uncertainty on C_{CO}. Deviations larger than our accuracy in estimating $F(t)$ have not been observed.

4 RESULTS   12

- $\tilde{A}$: The calculation of $\tilde{A}$ by Gaussian beam propagation is affected by a 5 % error due to uncertainty on pinhole size, focal length and position of lenses. However, deviations from the Gaussian spatial profile of the laser beam affect the estimation of the waist. Therefore we assess the error on $\tilde{A}$ in 10 %, which results in a 20 % uncertainty on C_{CO}.

Overall, considering also the error on $\sigma^{(2)}$, C_{CO} is estimated with a 60 % of uncertainty. C_{CO} represents the largest source of error on OH density estimation. C_{CO} is adjusted to OH LIF by multiplication with a calibration correction factor $\eta = 0.34 \pm 0.04$ accounting for the wavelength-dependent efficiencies of the optics, so that $C_{OH} = \eta C_{CO}$.

4.2 Building an OH calibration source

To realise the OH calibration source, the reactor is kept at a constant pressure of 100 mbar fed with He admixed with 0.25 % of water. A voltage of 4 kV is applied over the current-limiting 50 kΩ resistor and the plasma reactor. The power-supply is voltage-controlled. Helium's RET rate coefficient is large compared to its quenching rate coefficient resulting in rotational thermalization and the use of thermal rate coefficients from [36] is therefore justified.

In fig. 4 the OH fluorescence pulse measured in the new calibration source and its fit are shown. There is a little overshoot of the measured data (green points) at the beginning of the fluorescence pulse compared to the fitted decay (blue line), that was also observed in similar studies [36] and is attributed to scattered laser light that is not properly dispersed in the spectrometer. However, the general agreement is good as can be seen from the residual in the lower panel of fig. 4. An OH number density of $4 \pm 2 \times 10^{20} \, \text{m}^{-3}$ is obtained from the fit.

In the following, the validity of the underlying idea of the calibration, namely the agreement of the calibration constants for OH LIF and CO TALIF for a sufficiently good alignment, will be evaluated through comparing our results with other studies reporting OH number densities for similar amounts of water.

Among the available studies with similar water partial pressure often conditions are found that are too different from ours that a viable comparison is possible. Specifically, the studies have been conducted in pure water vapour [42] or He-H_2O with an equal share of water with respect to helium [43, 44]. Thereby, the measurements/simulations were done in molecular collisional environments in which systematically lower OH densities are reported.

Our conditions on the contrary are dominated by He. Kechidi, Belbachir, and Tahraoui come to a similar conclusion in the simulation of a capacitive discharge at 101.325 mbar consisting of 95 % He and 5 % H_2O [45]. This way, their conditions are the closest to ours among the discussed publications. Peak OH densities of $1 \times 10^{20} \, \text{m}^{-3}$ are calculated, thus in the same order as our results. Yonemori and Ono identify the upstream humidity of the He flow in a plasma jet as OH source [46]. With 100 ppm H_2O at atmospheric pressure about $6 \times 10^{18} \, \text{m}^{-3}$ OH are observed. As their water partial pressure is lower than in the present study, their work is in line with ours. In conclusion, the determined OH density is considered reasonable in the investigated He-dominated environment, especially regarding the error margin, thus approving the glow reactor as OH calibration source.
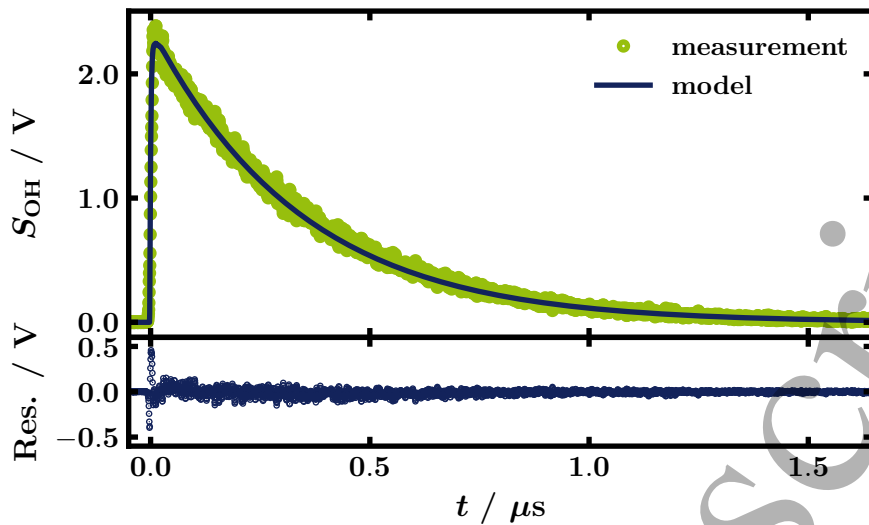
Figure 4: Fit of the fluorescence pulse of OH in the He-H_2O calibration source with the described model [28]. The lower panel shows the residual.

4.3 Results in a CO_2-H_2O discharge

The versatility of the calibrated LIF setup is demonstrated in a challenging molecular environment, namely a CO_2-H_2O glow discharge. The discharge is created in a gas mixture of 80 % CO_2 and 20 % H_2O at a pressure of 6.67 mbar. The voltage is controlled in such a way that at the end of the plasma pulse a current of 50 mA is reached. The results are summed up in fig. 5.

Panels a), c) and e) show how the rotational temperature of OH(X) T, the CO_2 conversion α defined in eq. (9) and the absolute OH number density ρ_{OH} are obtained from exemplary experimental observables, namely the excitation spectrum, fluorescence spectrum and fluorescence time evolution. To assess the quality of the fit/simulation the residual is plotted in the lower part of these panels. Accordingly, panels b), d) and f) show the time evolution of T, α and ρ_{OH} with respect to the plasma-on time that is indicated by a grey background.

4.3.1 Temperature

Panel a) shows an excitation spectrum that is obtained by integrating over time the fluorescence pulses for every laser excitation wavelength. The points are measured data while the solid line is the result of a simulation with LIFBASE assuming a thermal rotational distribution of the OH ground state [27]. The overall match between measurement and simulation is satisfying, enabling us to obtain an accurate rotational temperature T. In particular, the two peaks that are dominating the excitation spectrum for the given resolution, namely the $Q_1(6)$ line at 282.927 nm and the $Q_2(3)$ line at 282.937 nm, show good agreement with the simulation. Some small spectral features, e.g. on the left originating from the $Q_2(1)$ line at 282.923 nm, are not represented well. It might be an indication for being in the partially saturated regime. This possibility cannot be ruled out entirely since the saturation characteristics have not been checked for every measurement but is very unlikely since linearity was confirmed both for the calibration source and the CO_2-H_2O plasma at the beginning of the measurement campaigns. Additionally, a LIFBASE simulation of the same spectra assuming (partial) saturation affirmed the remaining in the linear regime because no better match could be obtained.

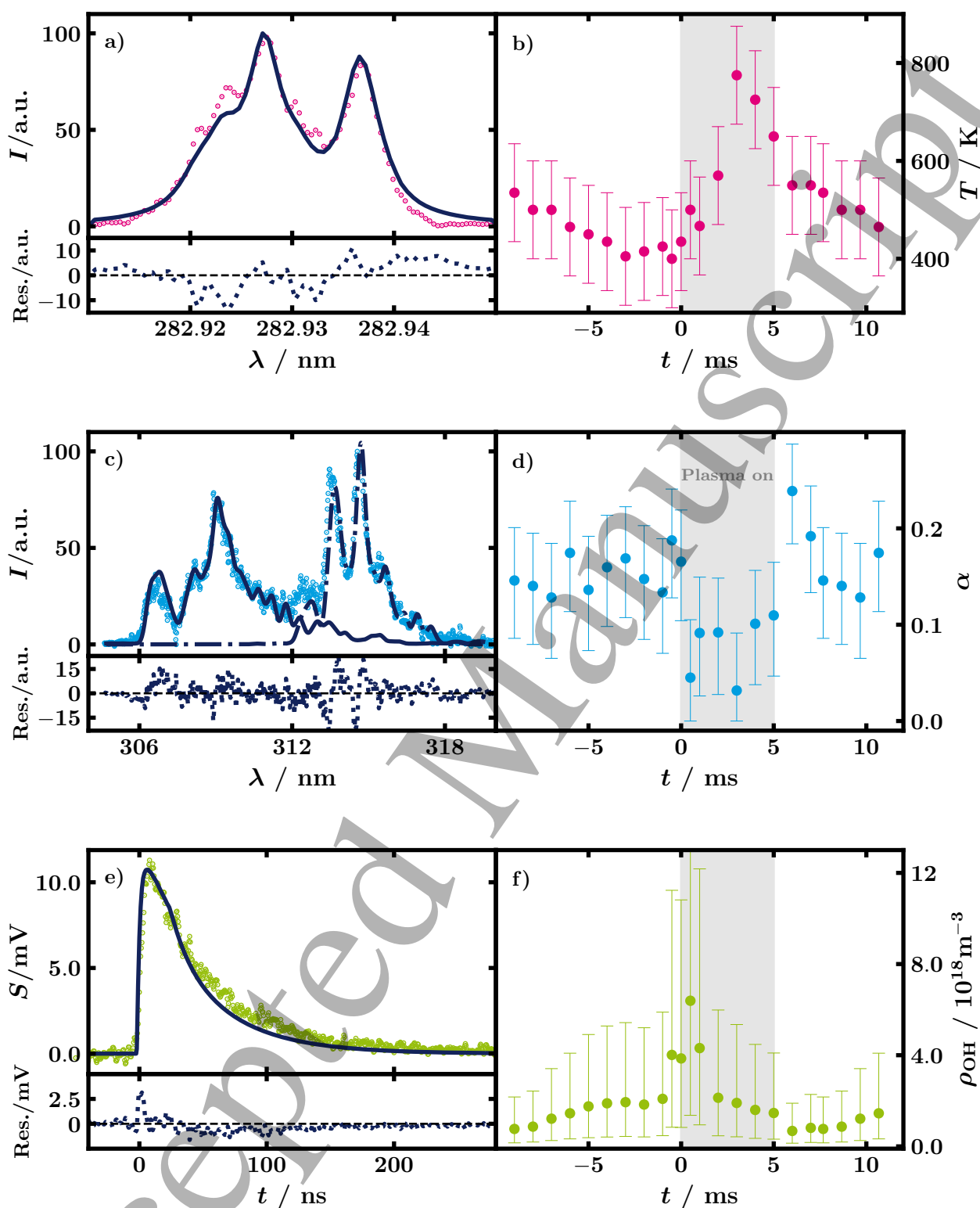4   RESULTS   14

Figure 5: Summary of the OH LIF measurements in the CO_2-H_2O glow discharge. Panels a), c) and e) show how the temperature, the band ratio or rather the conversion and the OH number density are obtained from the excitation spectrum, the fluorescence spectrum and the fluorescence pulse, respectively. The points are measured data while the lines are calculations. Below the residual is plotted to assess the quality of the fit/simulation. Panels b), d) and f) are plots of temperature, conversion and OH density against time with respect to the plasma pulse in grey. Error bars include statistical as well as systematic errors. See elaborations below for the details.

The mismatch between simulation and measurement could be explained by a distortion of the excitation spectrum that we attribute to overlap in excitation and detection wavelength between the 3064 Å system of OH and the third positive system of CO [27, 47]. The distortion becomes more severe when changing the experimental conditions, namely for smaller amounts of admixed water, which is the reason why we limit the current study to a relatively large water admixture of 20 %. Work on a future publication to clarify whether it is indeed the third positive system and how to minimise its influence on the measurement is in progress.

Furthermore, LIF thermometry in a molecular environment, characterised by high non-radiative quenching frequencies with respect to RET frequencies, can be less accurate in general. The excitation of different rotational states in the $OH(A, v' = 1)$ level by laser absorption results in different rotational population distribution functions in the $OH(A, v' = 1, 0)$ [35]. This implies that different non-radiative quenching frequencies must be used when exciting different rotational levels in the $OH(A, v' = 1)$ state, i.e. when collecting an excitation spectrum. The LIFBASE simulation software assumes by default no/constant quenching for the $OH(A, v' = 1)$ state, resulting in a less accurate simulation of the excitation spectrum. Also, a change in the gas composition, i.e. in the non-radiative quenching rate, can affect the accuracy of the temperature estimation [48]. To account for these inherent uncertainties the temperature values in fig. 5b) are presented with 2σ uncertainty.

The evolution of temperature over time is shown in panel b) of fig. 5. As expected, the gas cools down after the plasma pulse until 400 K when the next pulse begins. The plasma always stays above room temperature (even including error bars) as was observed in other studies with a comparable glow discharge as well [49]. When the plasma is on, a strong increase of the temperature until 800 K is observed. Interestingly, the temperature is not monotonically increasing until the end of the plasma pulse but shows a maximum at 3 ms, a behaviour that was confirmed by performing the same measurements several times. Although, the trend is not fully understood yet, it could be caused by the release of cold OH from the reactor walls, see the discussion of the absolute number density in section 4.3.3. To conclude, the temperatures themselves are in line with a previous comparable study with slightly lower water admixture [33] and are therefore considered valid. They are not only important for the further calculations in this paper but also an important input for chemical kinetic models.

4.3.2 Conversion

Here we show how from a measured fluorescence spectrum, and using the band ratio in eq. (8) we can determine the conversion. The fitted spectrum is shown in fig. 5c). According to the residual, the data is fitted well.

Panel d) displays the time evolution of the conversion. α lies between 5 and 25 % and is therefore larger than expected [33]. The deviation from the literature values is less severe considering the uncertainties introduced with water. To begin with, the amount of water is not measured in situ but determined by the performance of the evaporator that comes with uncertainty.

Next, the sensitivity of CET-LIF, i.e. the determination of the gas composition from the influence of the collisional environment on the OH fluorescence spectrum as explained in section 3.2, to the conversion of CO_2 decreases with water addition as pointed out by Gatti [50]. As can be seen in eq. (8), CET-LIF on OH is based on the change of the ratio of the rate coefficients for VET and quenching with the gas composition. For instance, pure CO_2 with a temperature of 800 K and by

using the non-thermal rate coefficients [35] has a coefficient ratio of about 1.3 leading to a prominent (0,0) band in the fluorescence spectrum. Since CO as well as O_2 have smaller coefficient ratios, CO_2 conversion leads to an overall ratio smaller than 1.3. However, H_2O has a smaller coefficient ratio than CO_2, too. A higher amount of water would have the same effect in the evaluation of the spectra as more conversion.

Additionally, it is worth noting that the derivation of the gas composition, i.e. CO_2 conversion, by the CET-LIF methodology assumes that the CO_2 splitting reaction takes place according to $2CO_2 \rightarrow 2CO + O_2$. Deviations from this stoichiometry, e.g. through the presence of atoms [51], could lead to under- or overestimation of the conversion. The quantification of this effect is difficult though, due to the lack of available rate coefficients for atoms.

Considering the uncertainty of the total amount of water for this analysis, a water percentage of 25 % rather than 20 % was assumed in fig. 5. The error bars are determined by running the fit with different reasonable amounts of water. They are manually shortened if they would reach below 0 % conversion. It is observed that the conversion while the plasma is off, is larger than inside the plasma pulse. This behaviour is counterintuitive since no energy is deposited. Nevertheless, a similar trend was observed in a TALIF spectroscopy study on CO [17] and a FTIR spectroscopy study [32] in a pure CO_2 pulsed DC glow discharge. The increase in conversion in the direct afterglow could be explained by vibrational up-pumping that is no longer prohibited by de-excitation through electron collisions [32]. In conclusion, the decrease of conversion in the plasma-on time is confirmed by three independent methods.

4.3.3   OH number density

Panel e) shows a measured fluorescence pulse as points and its corresponding fit as a line. The measured data is reasonably well fitted as can be seen by the residual. The time decay of the fluorescence is not fitted as well as in fig. 4 though. Probably, this is caused by the uncertainty in the gas composition mentioned before that influences the used total rates for quenching and VET.

The resulting OH number densities are shown in panel f). The error bars are obtained by varying the calibration constant C_{OH} which is the largest source of uncertainty. The first thing to note is the asymmetry of the error bars. This is because, in addition to the OH number density, the temperature and the pressure are used as fitting parameters in a small range around their nominal value, thus compensating for changes in the calibration constant. T can vary in the range of the error bars in panel b). The average pressure is kept constant by pumping through a feedback-controlled automatic valve. However, it has been shown that the pressure changes significantly on the millisecond timescale due to the gas expansion through heating [52]. Thus, the time-dependent pressure from Damen is used rather than the set pressure with a 20 % range of variation in the fit to account for differences in the conductivity of the gas lines with respect to the present setup [52]. Please note that the error bar at 0.5 ms that reaches up to $17 \times 10^{18} \, \mathrm{m}^{-3}$ is cut at the top for better visibility of the trend of the data points.

The observed number densities of about $1 \times 10^{18} \, \mathrm{m}^{-3}$ are two orders of magnitude lower than in the He-H_2O calibration source even though the water partial pressure is one order of magnitude higher. Apparently, the strongly quenching molecular environment hinders the OH production or promotes its destruction, as stated before in the assessment of the obtained number density in the calibration

4   RESULTS   17

source.

The measured OH density is lowest right after the plasma pulse and steadily increases until the start of the next pulse. This is caused by isobaric contraction since the average pressure is kept constant at 6.67 mbar while the temperature decreases as seen in fig. 5b) [17]. With the onset of the plasma, ρ_{OH} suddenly increases by a factor of three before sharply decreasing again within the plasma-on time. The increase in OH number density before the plasma started is probably due to a slight jitter in the ignition stage and is therefore considered an outlier.

Furthermore, one might ask why highly reactive OH is measured outside the plasma pulse when it is no longer produced through electron impact anyway. To answer the question, the rates of reactions that lead to the destruction of OH are evaluated. The largest rate coefficient belongs to the reaction of two OH molecules back to water and atomic oxygen, i.e. $1.8 \times 10^{-18} \, \mathrm{m^3 \, s^{-1}}$ at $400 \, \mathrm{K}$ [30], resulting in OH lifetimes of hundreds of milliseconds due to the low OH density, in agreement with the measurements. Another quite important reaction partner is CO, as stated in the introduction. Back reaction (1) at $400 \, \mathrm{K}$ has a rate coefficient of $1.57 \times 10^{-19} \, \mathrm{m^3 \, s^{-1}}$ [8] and reaction (2) is with $1.5 \times 10^{-18} \, \mathrm{m^3 \, s^{-1}}$ even comparable to the pure OH reaction [9]. We confirm the importance of these reactions since our measured OH density is lowest in times of highest conversion to CO, thus directly after the plasma pulse. Taking an average conversion of 0.15 and for comparability again a temperature of $400 \, \mathrm{K}$ leads to lifetimes of a few tens of microseconds. Even though long OH lifetimes were also observed in the afterglow of a nanosecond pulsed N_2-H_2O discharge [53] this cannot be brought in line with the present measurements.

Paradoxically, the explanation of the radiative behaviour of OH, i.e. CET-LIF, demands interaction of OH and CO while from a chemical standpoint the two molecules should rarely come in contact to explain the long lifetime of the hydroxyl radical. Obviously, not every collision of the two molecules results in a chemical reaction because otherwise the radiative effect would not be observable. An overestimation of the conversion, as was already indicated when comparing with literature values, eases but not fully solves the predicament.

There are two possible reasons for the observed behaviour:

(i) The CO is consumed by another reaction before it reacts with OH.

Regarding the large amount of admixed H_2O, the water-gas shift reaction $CO + H_2O \rightarrow CO_2 + H_2$ appears possible. The reaction usually relies on a catalyst to work efficiently. Although, a plasma can promote the reaction too, without the need for a catalyst, the temperature in the present study is too low for a significant influence of the water-gas shift reaction [54].

(ii) OH is supplied by a source other than the plasma.

According to Booth et al. the walls of a Pyrex tube like the used reactor are usually covered in OH groups. The surface groups are quite stable and are removed only at temperatures above about $800 \, \mathrm{K}$ [55]. From the results in fig. 5 the following mechanism could be inferred. With the plasma onset OH is produced through electron impact, see fig. 5f). At the same time the reactor gets heated up until a temperature of about $800 \, \mathrm{K}$ is reached, see fig. 5b). Cold hydroxyl groups from the surface get released and decrease the measured temperature. The decrease of OH density in fig. 5f) is flattened from an exponential-like decay to a more linear one. Furthermore, the production of OH and CO gets decoupled in time and space allowing the hydroxyl to survive longer. When assuming total surface coverage of $1 \times 10^{18} \, \mathrm{m^{-2}}$ [55] being released into the volume in the form of OH radicals, it would result

5 *CONCLUSION*   18

in a density change of roughly $2 \times 10^{20}\,\mathrm{m}^{-3}$ which is larger than the measured number density. Since this approximation is an upper limit for the released number of OH radicals it can be concluded that the surface can indeed influence the plasma significantly. To experimentally check this theory, it is possible to either cover the inner wall of the reactor with a material that does not offer chemisorption sites for hydroxyl groups [56] or to cool the reactor wall to prevent OH release due to heating [55, 57]. However, those measures obstruct the optical access needed for LIF measurements and are for that reason discarded in the present study. In summary, the presented time-dependent OH number density represents valuable input to validate modelling results. According to the proposed interpretation of the observed trend such a model should include reactions of OH with CO as well as the influence of the reactor walls on the plasma.

5 Conclusion

To the best of our knowledge absolute OH number densities were measured for the first time in a CO_2 pulsed DC glow discharge with water admixture. The influence of water addition on CO_2 plasmolysis is currently a hot topic due to water's potential to serve as abundant hydrogen source to form more complex molecules. In parallel, water is common impurity in industrial waste gas streams which makes the study of its impact compulsory from an application point of view.

A particularly important role falls to the highly reactive OH radical, e.g. through its capability to limit the effective conversion by back reaction with CO. The used LIF spectroscopy setup is calibrated by means of TALIF spectroscopy on CO to get absolute OH number densities in the range of $1 \times 10^{18}\,\mathrm{m}^{-3}$ in a CO_2 glow discharge with $20\,\%$ H_2O admixture at $6.67\,\mathrm{mbar}$ with a plasma current of $50\,\mathrm{mA}$. The trend of the OH number density emphasises the importance of reactions with CO but is not fully explained yet.

Additionally, the CO_2 conversion is estimated from the influence of the collisional environment on the OH spectra through CET-LIF. Counterintuitively, the conversion appears to be higher when the plasma is off, which is nevertheless in line with earlier studies. Finally, the rotational temperature of OH is determined by LIF thermometry and compared with previous measurements obtaining reasonable agreement.

With this powerful calibrated diagnostic at hand, a vast parameter space opens up for experimental studies. The absolute measures can be further used to assess the importance of certain reactions based on known reaction rates [58]. In the past, glow discharges have been shown to be well-suited for verification of kinetic models [59]. Knowledge of the OH density is expected to allow for the benchmarking of even more sophisticated simulations that include H_2O chemistry as well.

References

[1]   Goede, A P H 2018 *EPJ Web Conf.* **189**, 00010.

[2]   Snoeckx, R and Bogaerts, A 2017 *Chem. Soc. Rev.* **46**, 5805–5863.

[3]   Meunier, N, Laribi, S, Dubois, L, Thomas, D, and De Weireld, G 2014 *Energy Procedia* **63**, 6492–6503.

[4]   Hokazono, H and Obara, M 1990 *Appl. Phys. Lett.* **57**, 4–6.

[5]   Witteman, W J 1965 *Phys. Lett.* **18**, 125–127.

[6]   Witteman, W J and Goot, G V D 1966 *J. Appl. Phys.* **37**, 2919–2919.

[7]   Chen, G, Godfroid, T, Britun, N, Georgieva, V, Delplancke-Ogletree, M-P, and Snyders, R 2017 *Appl. Catal. B* **214**, 114–125.

[8]   Snoeckx, R, Ozkan, A, Reniers, F, and Bogaerts, A 2017 *ChemSusChem* **10**, 409–424.

[9]   Martini, L M, Gatti, N, Dilecce, G, Scotoni, M, and Tosi, P 2017a *Plasma Phys. Control. Fusion* **60**, 014016.

[10] Martini, L M, Lovascio, S, Dilecce, G, and Tosi, P 2018 *Plasma Chem. Plasma Process.* **38**, 707–718.

[11] Verreycken, T, Horst, R M van der, Baede, A H F M, Veldhuizen, E M van, and Bruggeman, P J 2012 *J. Phys. D* **45**, 045205.

[12] Wang, J, Simeni Simeni, M, Rong, M, and Bruggeman, P J 2021 *Plasma Sources Sci. Technol.*

[13] Nikiforov, A, Xiong, Q, Britun, N, Snyders, R, Lu, X P, and Leys, C 2011 *Appl. Phys. Express* **4**, 026102.

[14] Demtröder, W 2008 *Laser Spectroscopy: Vol. 1: Basic Principles* 4th ed. Berlin Heidelberg: Springer.

[15] Carrivain, O, Orain, M, Dorval, N, Morin, C, and Legros, G 2020 *Appl. Spectrosc.* **74**, 629–644.

[16] Seitzman, J M, Haumann, J, and Hanson, R K 1987 *Appl. Opt.* **26**, 2892–2899.

[17] Damen, M A, Hage, D A C M, Steeg, A W van de, Martini, L M, and Engeln, R 2019 *Plasma Sources Sci. Technol.* **28**, 115006.

[18] Grofulović, M, Silva, T, Klarenaar, B L M, Morillo-Candas, A S, Guaitella, O, Engeln, R, Pintassilgo, C D, and Guerra, V 2018 *Plasma Sources Sci. Technol.* **27**, 115009.

[19] Siegman, A E 1986 *Lasers* Mill Valley, Calif. : University Science Books.

[20] Bennett, K and Byer, R L 1980 *Appl. Opt.* **19**, 2408–2412.

[21] Klarenaar, B L M, Engeln, R, Bekerom, D C M van den, Sanden, M C M van de, Morillo-Candas, A S, and Guaitella, O 2017 *Plasma Sources Sci. Technol.* **26**, 115008.

[22] Tobias, I, Fallon, R J, and Vanderslice, J T 1960 *J. Chem. Phys.* **33**, 1638–1640.

[23] Fallon, R J, Tobias, I, and Vanderslice, J T 1961 *J. Chem. Phys.* **34**, 167–168.

[24] De Benedictis, S and Dilecce, G 2013 in: 261–284.

[25] Di Rosa, M D and Farrow, R L 1999 *J. Opt. Soc. Am. B* **16**, 1988–1994.

[26] McKenzie, R L and Gross, K P 1981 *Appl. Opt.* **20**, 2153–2165.

[27] Luque, J and Crosley, D R 1999 *SRI International Report MP.*

[28] Dilecce, G, Martini, L M, Tosi, P, Scotoni, M, and Benedictis, S De 2015 *Plasma Sources Sci. Technol.* **24**, 034007.

[29] Dieke, G H and Crosswhite, H M 1962 *J. Quant. Spectrosc. Radiat. Transf.* **2**, 97–199.

REFERENCES   20

[30] Verreycken, T, Horst, R M van der, Sadeghi, N, and Bruggeman, P J 2013   *J. Phys. D* **46**, 464004.

[31] Dilecce, G, Martini, L M, Ceppelli, M, Scotoni, M, and Tosi, P 2019   *Plasma Sources Sci. Technol.* **28**, 025012.

[32] Klarenaar, B L M, Morillo-Candas, A S, Grofulović, M, Sanden, M C M van de, Engeln, R, and Guaitella, O 2019   *Plasma Sources Sci. Technol.* **28**, 035011.

[33] Damen, M A, Martini, L M, and Engeln, R 2020   *Plasma Sources Sci. Technol.* **29**, 095017.

[34] Fridman, A 2008 *Plasma Chemistry* Cambridge University Press.

[35] Ceppelli, M, Martini, L M, Dilecce, G, Scotoni, M, and Tosi, P 2020   *Plasma Sources Sci. Technol.* **29**, 065019.

[36] Martini, L M, Gatti, N, Dilecce, G, Scotoni, M, and Tosi, P 2017b   *J. Phys. D* **50**, 114003.

[37] Di Teodoro, F, Rehm, J E, Farrow, R L, and Paul, P H 2000   *J. Chem. Phys.* **113**, 3046–3054.

[38] Settersten, T B, Dreizler, A, and Farrow, R L 2002   *The Journal of Chemical Physics* **117**, 3173–3179.

[39] Williams, L R and Crosley, D R 1996   *The Journal of Chemical Physics* **104**, 6507–6514.

[40] Xiong, Q, Nikiforov, A, Li, L, Vanraes, P, Britun, N, Snyders, R, Lu, X, and Leys, C 2012   *Eur. Phys. J. D* **66**.

[41] Dilecce, G, Ambrico, P F, and Benedictis, S De 2004   *Plasma Sources Sci. Technol.* **13**, 237–244.

[42] Avtaeva, S V, General, A A, and Kel'man, V A 2010   *J. Phys. D* **43**, 315201.

[43] Bernatskiy, A V, Ochkin, V N, and Kochetov, I V 2017   *Bull. Lebedev Phys. Inst.* **44**, 147–150.

[44] Wang, L, Deng, L, Li, B, Fang, B, Zhao, W, and Xu, H 2020   *Phys. Plasmas* **27**, 060701.

[45] Kechidi, Z, Belbachir, A H, and Tahraoui, A 2018   *Arab. J. Sci. Eng.* **43**, 361–372.

[46] Yonemori, S and Ono, R 2014   *J. Phys. D: Appl. Phys.* **47**, 125401.

[47] Krupenie, P H 1966 *The Band Spectrum Of Carbon Monoxide* Washington, D.C.: National Bureau of Standards.

[48] Ceppelli, M, Salden, A, Martini, L M, Dilecce, G, and Tosi, P 2021   *Plasma Sources Sci. Technol.*

[49] Grofulović, M, Klarenaar, B L M, Guaitella, O, Guerra, V, and Engeln, R 2019   *Plasma Sources Sci. Technol.* **28**, 045014.

[50] Gatti, N 2018 PhD Thesis University of Trento.

[51] Morillo-Candas, A S, Drag, C, Booth, J-P, Dias, T C, Guerra, V, and Guaitella, O 2019   *Plasma Sources Sci. Technol.* **28**, 075010.

[52] Damen, M A 2020 PhD Thesis Eindhoven University of Technology.

[53] Verreycken, T and Bruggeman, P J 2014   *Plasma Sources Sci. Technol.* **23**, 015009.

[54] Chen, W-H and Chen, C-Y 2020   *Appl. Energy* **258**, 114078.

[55] Booth, J-P, Guaitella, O, Chatterjee, A, Drag, C, Guerra, V, Lopaev, D, Zyryanov, S, Rakhimova, T, Voloshin, D, and Mankelevich, Y 2019   *Plasma Sources Sci. Technol.* **28**, 055005.

[56] Morillo-Candas, A S, Klarenaar, B L M, Amoedo, C, Guerra, V, and Guaitella, O 2020   *J. Phys. D: Appl. Phys.* **54**, 095208.

[57] Ogloblina, P, Morillo-Candas, A S, Silva, A F, Silva, T, Caz, A Tejero del, Alves, L L, Guaitella, O, and Guerra, V 2021   *Plasma Sources Sci. Technol.* **30**, 065005.

REFERENCES   21

[58]   Brisset, A, Gibson, A R, Schröter, S, Niemi, K, Booth, J-P, Gans, T, O'Connell, D, and Wagenaars, E 2021   *J. Phys. D* **54**, 285201.

[59]   Silva, T, Grofulović, M, Klarenaar, B L M, Morillo-Candas, A S, Guaitella, O, Engeln, R, Pintassilgo, C D, and Guerra, V 2018   *Plasma Sources Sci. Technol.* **27**, 015019.